

Published in final edited form as:

*Magn Reson Med.* 2006 July ; 56(1): 94–103. doi:10.1002/mrm.20926.

## Designing Long- $T_2$ Suppression Pulses for Ultrashort Echo Time Imaging

Peder E. Z. Larson<sup>1,\*</sup>, Paul T. Gurney<sup>1</sup>, Krishna Nayak<sup>2</sup>, Garry E. Gold<sup>3</sup>, John M. Pauly<sup>1</sup>, and Dwight G. Nishimura<sup>1</sup>

<sup>1</sup>Magnetic Resonance Systems Research Laboratory, Department of Electrical Engineering, Stanford University, Stanford, California, USA

<sup>2</sup>Magnetic Resonance Engineering Laboratory, Department of Electrical Engineering, University of Southern California, Los Angeles, California, USA

<sup>3</sup>Department of Radiology, Stanford University, Stanford, California, USA

### Abstract

Ultrashort echo time (UTE) imaging has shown promise as a technique for imaging tissues with  $T_2$  values of a few milliseconds or less. These tissues, such as tendons, menisci, and cortical bone, are normally invisible in conventional magnetic resonance imaging techniques but have signal in UTE imaging. They are difficult to visualize because they are often obscured by tissues with longer  $T_2$  values. In this article, new long- $T_2$  suppression RF pulses that improve the contrast of short- $T_2$  species are introduced. These pulses are improvements over previous long- $T_2$  suppression pulses that suffered from poor off-resonance characteristics or  $T_1$  sensitivity. Short- $T_2$  tissue contrast can also be improved by suppressing fat in some applications. Dual-band long- $T_2$  suppression pulses that additionally suppress fat are also introduced. Simulations, along with phantom and in vivo experiments using 2D and 3D UTE imaging, demonstrate the feasibility, improved contrast, and improved sensitivity of these new long- $T_2$  suppression pulses. The resulting images show predominantly short- $T_2$  species, while most long- $T_2$  species are suppressed.

### Keywords

ultrashort echo time (UTE) imaging; long- $T_2$  suppression;  $T_2$  contrast; short- $T_2$  imaging; RF pulse design

---

Ultrashort echo time (UTE) imaging is a novel type of magnetic resonance imaging (MRI) that can image tissues with very short  $T_2$  relaxation times. These tissues are normally invisible in all other types of MRI. There are many potential in vivo applications imaging short  $T_2$  species (1), including collagen-rich tissues such as tendons, ligaments, and menisci, as well as calcifications, myelin, periosteum, and cortical bone.

Conventional imaging methods have minimum echo time (TE) requirements and thus can only image species with  $T_2$  values greater than a few milliseconds. UTE imaging, as well as single-point imaging methods such as SPRITE (3) and related multipoint methods (4), begin acquiring data as soon as possible after excitation. In these methods, the TE is limited only by how quickly the MR system can switch from transmit to receive mode, which depends on electronics

switching times as well as coil ring-down time. On present-day clinical MR systems the minimum switching time is about 60–200  $\mu\text{s}$ , with the shortest TE reported on a clinical 1.5 T system being 8  $\mu\text{s}$  (5).

Previous studies have explored many UTE imaging applications. These include imaging calcifications, cavernomas, and metastases in the brain (6,7), hemochromatosis and cirrhosis in the liver (8), periosteum (9), lung parenchyma (10,11), tendons and menisci (12), the Achilles' tendon (13), and articular cartilage (14). Recent studies have also investigated using gadolinium for contrast enhancement (15), as well as short- $T_2$  phosphorus imaging in vivo (16). UTE imaging has also been applied to chemical shift imaging (17) and spectroscopy (14), as well as angiography (18) and temperature mapping in frozen tissue (19). Connective structures such as myelin, capsules, and falx are other potential areas for UTE applications.

Short- $T_2$  species in UTE imaging often suffer from poor contrast. This is due to surrounding long- $T_2$  tissues with high signal or overlapping long- $T_2$  components that obscure the short- $T_2$  components. In general, the longer  $T_2$  species will have higher signal since they decay slower and thus are easier to image. Long- $T_2$  suppression is an important technique that improves the contrast and visualization of short- $T_2$  components.

Multiple methods have been proposed for long- $T_2$  suppression, all of which can be classified into two groups. The first group consists of methods that combine images acquired with different TEs to create  $T_2$  contrast. The most common technique is to subtract a later echo image, containing signal only from long- $T_2$  species, from the first echo image (1). Combining multiple different TE images can also create highly  $T_2$  selective images without the need for  $T_2$  fitting (20). Image combination long- $T_2$  suppression techniques are simple to implement and provide a reference image that is useful for diagnosis. The short- $T_2$  signal-to-noise ratio (SNR) is decreased by the combination, and artifacts due to off-resonance and  $T_2^*$  effects are a problem.

The other group of long- $T_2$  suppression methods are based on RF pulses. The original method prepares the magnetization with a long rectangular  $\pi/2$  pulse followed by a dephaser (21). Short- $T_2$  species are not excited by the pulse because the decay rate exceeds the excitation rate while long- $T_2$  species are saturated, creating  $T_2$  contrast. This technique is SNR and contrast efficient, but is very sensitive to off-resonance and inhomogeneous  $B_1$  fields, and does not suppress fat. Another technique, called refocused TELEX, was designed to highlight longer short- $T_2$  species ( $> 10$  ms) (22). The method uses a long  $\pi/2$  pulse routinely interrupted by refocusing pulses to improve the off-resonance characteristics of the suppression. Its performance varies with  $T_1/T_2$ .

Inversion recovery (IR) can also be used to selectively null long- $T_2$  components with a particular  $T_1$  (1). A longer duration inversion pulse will not affect short- $T_2$  species too much but will have a narrow spectral bandwidth. This technique is  $T_1$  selective.

Fat suppression is also useful in UTE when imaging short- $T_2$  components that are surrounded by fat, such as tendons, ligaments, menisci, periosteum, and cortical bone. Conventional techniques, such as fat-selective saturation pulses, IR, and Dixon techniques (12), have all been used in UTE imaging. Each of these methods can be applied in addition to long- $T_2$  suppression.

In this article we describe a new set of RF pulses for long- $T_2$  suppression. These pulses are more robust to off-resonance than long rectangular pulses without introducing  $T_1$  selectivity or compromising short- $T_2$  signal levels. We also introduce a new set of dual-band pulses that include long- $T_2$  suppression at both the water and the fat resonances.

## THEORY

Long- $T_2$  suppression pulses are based on the observation that it is easy to excite long- $T_2$  species but difficult to excite short- $T_2$  species. Short- $T_2$  species aren't affected by low-amplitude, long-duration pulses because their transverse magnetization decays faster than it is excited. As  $T_2$  increases, the excitation rate dominates the transverse relaxation. Thus, long- $T_2$  species are fully excited and short- $T_2$  species are relatively unaffected.

When  $T_2$  is much greater than the pulse duration ( $T_{\text{pulse}}$ ) and the excitation rate dominates the transverse relaxation, we can analyze the suppression pulses using standard tools such as the Shinnar–Le Roux (SLR) transform (23).

When  $T_2$  is on the order of or less than  $T_{\text{pulse}}$ , the transverse relaxation can no longer be neglected. In this case, we do simulations and analysis with the Bloch equation. To simplify the analysis, we assume that the spins are on-resonance, the RF pulse is amplitude modulated, and we neglect  $T_1$  relaxation. The Bloch equation in the rotating frame is reduced to two differential equations:

$$\frac{dM_y(t, T_2)}{dt} = \frac{-M_y(t, T_2)}{T_2} + \omega_1(t)M_z(t, T_2) \quad [1]$$

$$\frac{dM_z(t, T_2)}{dt} = -\omega_1(t)M_y(t, T_2), \quad [2]$$

where  $\omega_1(t) = \gamma B_1(t)$  is the RF pulse. Using the small-tip approximation ( $M_z(t, T_2) \approx M_0$ ), a solution for  $M_y(t, T_2)$  can be derived, similar to the proof in (24):

$$M_y(t, T_2) = M_0 \int_0^t e^{-(t-s)/T_2} \omega_1(s) ds. \quad [3]$$

[Equation 3] expresses  $M_y(t, T_2)$  as a convolution of  $\omega_1(t)$  and a truncated  $e^{-t/T_2}$ , illustrated in Fig. 1. A useful simplification can be made for short enough  $T_2$  values such that the RF pulse is slowly varying relative to the exponential weighting,  $e^{-t/T_2}$ . A pulse with a bandwidth, BW, will have oscillations on the time scale of  $1/\text{BW}$ , while the exponential weighting is mostly decayed within time  $T_2$ . The condition for making this simplification is that  $T_2 \ll 1/\text{BW}$ , or  $T_2 \times \text{BW} \ll 1$ . We can then remove  $\omega_1(t)$  from the integral in Eq. [3] since it is approximately constant during the exponential weighting, allowing us to derive the following approximate solution for  $M_y(t, T_2)$ :

$$M_y(t, T_2) \approx M_0 \int_0^t e^{-(t-s)/T_2} ds \cdot \omega_1(t) \quad [4]$$

$$= M_0 T_2 (1 - e^{-t/T_2}) \cdot \omega_1(t) \quad [5]$$

$$\approx M_0 T_2 \cdot \omega_1(t). \quad [6]$$

This result indicates how short- $T_2$  species decay faster than excited and also that the transverse magnetization is approximately proportional to  $T_2$  when  $T_2 \times \text{BW} \ll 1$ .

Finally, we revisit the longitudinal magnetization and refine our model by assuming that it is not constant.  $M_Z(t, T_2)$  is then solved by substituting the result from Eq. [6] into Eq. [2]. After integrating the differential equation to the end of the pulse,  $t = T_{\text{pulse}}$ , with the initial condition that  $M_Z(0, T_2) = M_0$ , the resulting longitudinal magnetization is

$$M_Z(T_{\text{pulse}}, T_2) \approx M_0(1 - T_2 \int_{-\infty}^{\infty} \omega_1(t)^2 dt), \quad [7]$$

with  $\omega_1(t) = 0$  for  $t < 0$  and  $t > T_{\text{pulse}}$ . The change in  $M_Z$  is proportional to  $T_2$  multiplied by the RF power, irrespective of the pulse shape. We will use this flexibility in designing the suppression pulses.

We can gain more insight by applying Rayleigh's Theorem to Eq. [7]:

$$M_Z(T_{\text{pulse}}, T_2) \approx M_0(1 - T_2 \int_{-\infty}^{\infty} |\Omega_1(f)|^2 df), \quad [8]$$

where  $\Omega_1(f)$  is the Fourier transform, or frequency spectrum, of the RF pulse. This shows a trade-off between total RF spectral power and short- $T_2$  attenuation.

Equation [8] can also be understood in terms of spectral linewidths.  $T_2$  is inversely proportional to the linewidth, meaning that short- $T_2$  species have broad linewidths and long- $T_2$  species have narrow linewidths. The overlap between the spectrum of the RF pulse and the tissue spectrum determines the excitation, shown in Fig. 2. The narrow spectrum of a long- $T_2$  species is more easily covered by the RF spectrum and thus is easily excited. (This result is also derived in (22).) The broad short- $T_2$  species spectrum requires a wide bandwidth RF pulse to be excited. A narrow bandwidth RF pulse will fully excite the longer  $T_2$  species but only partially excite the shorter  $T_2$  species, making it an effective long- $T_2$  suppression pulse.

Main magnetic field inhomogeneity causes resonance shifts in protons.  $T_2^*$  includes the effects of these shifts when summed over a tissue or voxel. For short- $T_2$  species, these shifts are generally small relative to the linewidth, so the field inhomogeneity does not affect the preceding analysis. Resonance shifts on the order of the pulse bandwidth will compromise the suppression of long- $T_2$  species, as shown in the Results.

## METHODS

### Pulse Design

Equation [8] shows that short- $T_2$  attenuation is approximately linear with pulse bandwidth. This means that long- $T_2$  suppression pulses will be limited in bandwidth, but carefully choosing how this bandwidth is used will reduce off-resonance sensitivity. Desirable spectral profile characteristics are flat suppression bands, short transition widths, and minimal excitation out of the suppression band. The flat suppression band will suppress long- $T_2$  species at a wide range of resonances, while a short transition width and minimal out-of-band excitation will reduce undesired short- $T_2$  attenuation. The SLR pulse design algorithm is well suited to long- $T_2$  suppression pulse design because it can produce the desired spectral profile characteristics and the resulting pulses are minimum power for a chosen profile (23).

Suppression, or saturation, pulses do not require a linear phase and will benefit from having nonlinear phase, which allows for shorter transition bands and also introduces phase dispersion

into the saturated magnetization. We achieve nonlinear phase by first designing a linear phase filter using Parks–McClellan digital filter design algorithms (25). The filter roots are manipulated to produce a maximum-phase pulse, as described in (23). The resulting maximum-phase filter is converted to an RF pulse using the SLR transform. Using other nonlinear phase profiles is not necessary because they will not improve the spectral or  $T_2$  profile and peak power is not a concern for these low-amplitude pulses.

### Single-Band Pulses

Single-band long- $T_2$  suppression pulses have one spectral saturation band to suppress long- $T_2$  species on the water proton resonance. These are maximum-phase saturation pulses created using the SLR pulse design algorithm with Parks–McClellan filter design, as described in (23).

The primary design parameter is the time  $\times$  bandwidth product (TBW), which is proportional to the spectral profile sharpness. The bandwidth in the TBW product is the full-width, half-maximum (FWHM) bandwidth of the filter, which corresponds to the  $M_Z = 0.75 M_0$  bandwidth of a saturation pulse and is also proportional to the short- $T_2$  attenuation. The FWHM bandwidth ( $BW_{FWHM}$ ) is wider than the range of off-resonances that will be adequately suppressed. A few rules of thumb for a given  $BW_{FWHM}$  are that  $T_2$  (ms) = 2000/ $BW_{FWHM}$  (Hz) will be reduced to 10% of its initial magnetization, while  $T_2 = 1000/BW_{FWHM}$  will be at 20% and  $T_2 = 300/BW_{FWHM}$  at 50% of their initial magnetizations.

The TBW product is a trade-off between the pulse duration and profile sharpness since the FWHM bandwidth is generally constrained by the desired short- $T_2$  response and/or expected off-resonances. Rectangular suppression pulses are  $TBW \approx 1$ , resulting in a poor profile but a short pulse length. We have generally used pulses with a TBW between 2 and 3, as they have a reasonably flat spectral profile, which is a significant improvement on the rectangular pulse profile. Higher TBW pulses have slightly sharper profiles but they must be longer, during which  $T_1$  relaxation effects may compromise the suppression. A single-band pulse with TBW of  $N$  must be  $N$  times as long as a rectangular pulse to have the same  $T_2$  response. We have primarily used single-band pulses between 10 and 40 ms in length.

The other design parameters are the passband and stopband ripples and the filter order. Ripple values of 1% are sufficient for these pulses. We used a filter order of 250, but this is more than necessary and orders as low as 20 would probably be sufficient. A pulse designed with a given TBW can be stretched in time to change the  $T_2$  response and FWHM bandwidth.

### Dual-Band Pulses

Dual-band long- $T_2$  suppression pulses have two spectral saturation bands at the fat and water resonances to suppress long- $T_2$  species at both resonances. They are created by first designing a dual-band filter using the complex Parks–McClellan algorithm (26). The resulting equiripple linear phase filter is converted into a maximum-phase filter, which is transformed to an RF pulse using the SLR transform.

The design parameters are the pulse duration, suppression bandwidths, fat band frequency offset, filter order, and desired ripple values. The suppression bandwidths are not FWHM bandwidths and instead correspond to the actual range of off-resonances suppressed. Typically we use suppression bandwidths of 60 to 100 Hz on-resonance and 80 to 150 Hz at the fat resonance, which is centered around  $-220$  to  $-260$  Hz. A filter order of 100 to 200 and ripple values of 0.5% are adequate. The pulses require 20 to 30 ms, and longer durations will result in narrower transition widths. The transition width is calculated as  $\Delta f = D_{inf,m}(\delta_1, \delta_2)/T_p$ , where  $T_p$  is the pulse length,  $\delta_1$  and  $\delta_2$  are the suppression band and out-of-band ripples values, and

$D_{\text{inf},m}(\delta_1, \delta_2)$  is defined in (23). Transition widths between 30 and 60 Hz are typical. Narrower transition regions will result in slightly less short- $T_2$  attenuation.

### Sample Pulses

Figure 3 shows three long- $T_2$  suppression pulses used in both phantom and in vivo experiments. The 16-ms rectangular and 40-ms TBW = 2.4 single-band pulse have approximately identical  $T_2$  profiles, with FWHM bandwidths of 62.5 and 60 Hz, respectively. The 25-ms dual-band pulse was designed with suppression bandwidths of 80 Hz on-resonance and 140 Hz centered at  $-255$  Hz off-resonance for fat suppression.

The long- $T_2$  suppression pulses were designed in Matlab 7.0 (The Mathworks, Natick, MA, USA). The design functions, accompanying documentation, and sample pulses are available for general use at <http://www-mrsrl.stanford.edu/~peder/longt2supp>.

### Simulations

To initially validate the performance of the RF pulses, we simulated their off-resonance and  $T_2$  profiles. We used a Bloch equation simulation that calculates the precession and decay matrices using the RF waveforms for each of a set of resonant frequencies. This Bloch simulation was coded in Matlab and is available at <http://www-mrsrl.stanford.edu/~brian/blochsim>. Off-resonance simulations used  $T_2 = 100$  ms,  $T_1 = 1$  s, and frequencies relative to water protons at 1.5 T.

### Experiments

A GE Excite 1.5 T scanner with gradients capable of 40 mT/m amplitude and 150 T/m/s slew rate (GE Healthcare, Milwaukee, WI, USA) was used for all experiments. The minimum TE of our configuration was 80  $\mu$ s, limited by the coil ring-down time and hardware switching times.

Both 2D and 3D UTE sequences were used. A 2D sequence is shown in Fig. 4. The long- $T_2$  suppression pulses and an accompanying dephaser gradient were applied as contrast preparation before the imaging sequences. A halfpulse excitation was used in the 2D sequence, where two acquisitions with alternating slice select gradients are summed to obtain the full-pulse slice profile (10,11). A slice prephasing gradient was also used to eliminate spatially dependent phase terms that arise when acquiring off-isocenter slices. Without this prephaser, these phase terms will distort the slice profile when the two acquisitions are summed.

The 3D sequence does not require slice-selective excitation and instead uses a hard pulse. This eliminates several problems associated with half-pulses, including sensitivity to timing errors, eddy current artifacts (19), compromised slice profiles for short- $T_2$ s, and large excitation tails that make multislice scanning difficult. The 3D acquisition requires a longer scan time and shimming over a large volume.

A projection reconstruction (PR) radial readout with a 125- or 250-kHz sampling bandwidth was used in the 2D imaging to acquire the quickly decaying short- $T_2$  data as rapidly as possible. We limited the acquisition time to 1 ms. In 3D imaging we used a twisted 3D PR trajectory that is significantly faster than 3D PR while maintaining the field of view (FOV) and resolution (27). The repetition time (TR), number of readouts, and samples per readout varied across experiments.

$T_2$  phantoms were created by doping distilled water with manganese chloride ( $\text{MnCl}_2$ ), resulting in  $T_2/T_1$  values of 0.3/2, 0.6/4, 1.2/7, 2.4/15, 4/30, 4.8/35, 6/40, 10/70, 20/100, 50/250, and 100/460 ms. They were imaged using a 2D UTE sequence with TE = 80  $\mu$ s, flip angle =



60°, 5-mm slice thickness, 1-mm in-plane resolution, and TR = 200 ms, 1 s, or 2 s, chosen such that  $TR \geq 4 \times T_1$ . A transmit/receive head coil was used.

Off-resonance data was acquired with the  $T_2/T_1 = 100/460$  ms phantom by applying linear gradients to induce resonance shifts, which were quantified using a field map. Many of the phantoms experienced nonnegligible  $T_1$  recovery because their  $T_1$  was on the order or less than the suppression pulse durations. The  $T_1$  recovery was compensated for in postprocessing using the pulse durations and the delay between suppression and excitation.

In vivo experiments were performed on healthy volunteers. All subjects gave informed consent in accordance with Stanford University policy after they were screened for possible MRI risk factors. Brain images were acquired with a 2D UTE sequence with TE = 80  $\mu$ s, TR = 500 ms, flip angle = 60°, 4:15 per image, 5-mm slice thickness, and 1-mm in-plane resolution. Later TEs of 2.3, 4.7, and 9.4 ms were also acquired to create field maps and subtraction images. A transmit/receive head coil was used. 3D UTE imaging was done on the ankle and knee with 0.6-mm isotropic resolution, TR = 100 ms, TE = 80  $\mu$ s, and a 7-cm FOV. A total of 12000 spokes of a twisted 3D PR trajectory were acquired in 20 min of total scan time. Ankle imaging was done with a 3-inch surface coil. Knee images were acquired using a transmit/receive extremity coil. Shimming for 3D acquisitions was done manually using a quickly acquired field map.

The bandwidth of the long- $T_2$  suppression pulses was chosen based on the desired application. In the brain we found that  $\pm 15$  Hz of suppression bandwidth was necessary for a single slice; thus, we chose a 40-ms TBW = 2.4 single-band suppression pulse, shown in Fig. 3b, and compared it to a 16-ms rectangular pulse, shown in Fig. 3a. In the ankle and knee we needed at least  $\pm 30$  Hz suppression bandwidth for the volume, so we used a 25-ms dual-band pulse with  $\pm 40$  Hz suppression bandwidth at water and  $\pm 70$  Hz centered around  $-255$  Hz for fat suppression (Fig. 3c).

## RESULTS

### Simulations

Figure 5 compares the relationship derived in Eq. [7] with simulations over a range of short- $T_2$  values for three different pulse shapes: a 16-ms rectangular pulse, a 32-ms TBW = 2 pulse, and a 64-ms TBW = 4 pulse, each of which have a FWHM bandwidth = 62.5 Hz. There is reasonable agreement for each of these pulses in the shown time scale, which has a maximum  $T_2 \times BW \approx 0.03 \ll 1$ , satisfying the approximation used to derive Eq. [7]. The agreement degrades as  $T_2$  increases because this condition is violated.

The Bloch equation simulation results in Fig. 6 confirm the relation between pulse bandwidth and longitudinal magnetization after suppression derived in Eq. [8]. As the pulse bandwidth increases, the remaining signal decreases, as expected, with varying rates depending on  $T_2$ . Also as expected, the remaining signal decreases as  $T_2$  increases. Note that the different  $T_2$  curves are simply shifted versions of each other, meaning that the remaining magnetization will be approximately constant for a constant  $T_2 \times BW$  product. This product shows up in Eq. [8] as  $T_2 \int_{-\infty}^{\infty} |\Omega_1(f)|^2 df$ .

Figure 7 compares the 16-ms rectangular and 40-ms TBW = 2.4 single-band suppression pulses shown in Figs. 3a and b. The  $T_2$  profiles are nearly identical, as we expect because the pulses have similar FWHM bandwidths of 62.5 and 60 Hz, respectively. They both retain 90% of the initial magnetization for  $T_2 = 600$   $\mu$ s, 50% for  $T_2 = 5$  ms, and 10% for  $T_2 \approx 30$  ms. The single-band pulse has an improved off-resonance profile, with a factor of 20 suppression bandwidth of 30 Hz, compared to 10 Hz for the rectangular pulse. This is approximately a factor of 3

improvement without compromising the short- $T_2$  attenuation. The rectangular pulse wastes power in its wide transition region and passband ripples, seen around  $\pm 90$  Hz in Fig. 2b.

When a second band for long- $T_2$  fat suppression is added to the pulses, we expect to see an increase in short- $T_2$  attenuation. Figure 8 compares the 25-ms dualband pulse from Fig. 3c (solid line) to a 25-ms dual-band pulse with a narrower fat suppression band (dashed line) and a 25-ms TBW = 3.4 single-band pulse (dotted line). The water-resonance  $T_2$  profile in Fig. 8a shows this increase in short- $T_2$  attenuation in the dual-band pulses. All three pulses have a factor of 20 suppression bandwidth of 80 Hz on-resonance, and the single-band pulse has a FWHM bandwidth of 136 Hz. Widening the fat suppression band has only a small effect on short- $T_2$  species while reducing the chance of fat suppression failure due to off-resonance.

## Experiments

Data from  $T_2$  phantom experiments is plotted with the simulated  $T_2$  and off-resonance profiles in Figs. 7 and 8. The off-resonance data in Fig. 2b agrees excellently with the simulated results for both pulses. There is also excellent agreement in Fig. 2a for the 40-ms TBW = 2.4 suppression pulse ( $\times$ ). The 16-ms rectangular pulse data (+) shows some disagreement, especially at  $T_2 = 20$  and 50 ms. This could be the result of averaging over small resonance shift ranges, which would increase the signal because of the narrow suppression bandwidth. The phantom data in Fig. 8 were acquired using the 25-ms dualband pulse from Fig. 3c. Both the on-resonance  $T_2$  data and off-resonance data agree well with the simulated results.

Figures 9 and 10 show brain UTE images with and without long- $T_2$  suppression for two different volunteers. The use of long- $T_2$  suppression pulses reveals a white matter short- $T_2$  component that is completely obscured without suppression. We believe that this component is associated with myelin, as has previously been suggested by its absence in patients with multiple sclerosis (1,7). Short- $T_2$  components in the falx cerebri (long, thin arrows in Fig. 9) also have significantly improved visualization with suppression. The rectangular and single-band long- $T_2$  suppression pulses have identical  $T_2$  profiles, and thus they produce similar contrast.

The rectangular pulse suppression (Figs. 9b and 10d) produces varying contrast across the image and poorer delineation of the white matter short- $T_2$  component than the single-band pulse suppression (Figs. 9c and 10e). There are areas of signal dropout and failed suppression, indicated by the short, fat arrows. These failures are likely due to the narrow bandwidth of the rectangular suppression pulse, similar to the suppression failures observed in longer  $T_2$  phantoms in Fig. 7a. The field map in Fig. 10c corroborates this claim, as the suppression failures with the rectangular suppression pulse in Fig. 10d correlate with the largest off-resonance frequencies. As the off-resonance approaches  $\pm 20$  Hz, the suppression fails, as we would expect from the results in Fig. 7b.

Long- $T_2$  suppression with the single-band pulse is more consistent due to its improved off-resonance profile, resulting in clear and consistent delineation of the white matter short- $T_2$  component. Subtracting a TE = 9.7 ms image from the TE = 80  $\mu$ s image (Fig. 10a) produces the image shown in Fig. 10c. This result shows the falx cerebri but the visualization of the short- $T_2$  component in the white matter is poor and inconsistent. Previous brain UTE studies have produced more promising image subtraction results, sometimes in conjunction with IR to null the long- $T_2$  white matter component for improved contrast (1,7). In all of our experiments, the short- $T_2$  component delineation is clearer when using a single-band suppression pulse, as opposed to subtraction or a rectangular suppression pulse.

Ankle images acquired with and without a dual-band long- $T_2$  suppression pulse are shown in Fig. 11. The muscle and fat are well suppressed by the dual-band pulse. The Achilles' tendon,



measured to have two short- $T_2$  \* components of 0.53 (88%) and 4.80 ms (12%) posteriorly and 0.60 (70%) and 4.20 ms (30%) anteriorly (13), is extremely visible in Fig. 11b (long, thin arrow). It is visible again in Fig. 11d, as are the peroneal, flexor hallucis longus, flexor digitorum longus, and tibialis posterior tendons (long, thin arrows). Additionally, the plastic in the boot bracing the foot can be seen (long, dashed arrow). There is still some signal remaining in the fat pad anterior to the Achilles' tendon (short, dashed arrow in Fig. 11b), which may be due to failed suppression or short- $T_2$  components in the fat. There is also strong signal posterior to the Achilles' tendon (short, solid arrow in Fig. 11b), which may be from the collagen in the skin or an off-resonance artifact due to susceptibility differences at the air-tissue interface.

The knee images in Fig. 12 show similar improvements in short- $T_2$  contrast when a dual-band suppression pulse was applied. The patellar tendon and menisci have significantly improved contrast in Figs. 12b, c, and d (long, thin arrows). Figure 12d shows the iliotibial band and anterior cruciate ligament (dashed arrows), as well as thickened tibial cortex in the weight-bearing region of the knee (double arrow). Resonance shifts caused the suppression to fail in the fat near the patella (a common location of fat-saturation failure) and posterior to the femoral condyles, seen in Fig. 12b (short, fat arrows). Note that the cartilage, generally thought of as a short- $T_2$ , is suppressed since it has a  $T_2$  around 25–45 ms (28).

## DISCUSSION

The dual-band and single-band long- $T_2$  suppression pulses generate excellent short- $T_2$  contrast and reveal short- $T_2$  components obscured by long- $T_2$  components. They show promise for use in UTE imaging.

The primary difficulty in applying the single and dual-band long- $T_2$  suppression pulses is due to the trade-off between short- $T_2$  signal and bandwidth. Since we wanted to maximize both, we often pushed the limits of the shimming system to increase short- $T_2$  signal, making off-resonance artifacts more likely. Choosing the appropriate pulse bandwidth is difficult and will differ by imaging application. For example, extremity imaging has more susceptibility artifacts at tissue-air interfaces and will require a larger bandwidth, whereas brain tissue is more uniform and can tolerate a narrower bandwidth.

The range of short- $T_2$  values for which we expect this technique to perform well for is limited due to this trade-off. With our technique, tissues with  $T_2$  values less than a few milliseconds will have relatively good signal. We expect to be able to image tissues with higher  $T_2$  values, up to about 10 ms, but the suppression pulses may attenuate the signal. Tissues with  $T_2$  values longer than about 10 ms will be difficult to image unless the main magnetic field is very uniform across the area of interest.

For the reasons just described, a good shim significantly improves image quality. In our 3D imaging experiments we acquired a 3D field map and then manually adjusted the shim coils. This was especially useful for 3D volumes in the foot and knee, where there is significant resonance frequency variation. Only a couple minutes were required to complete this process.

The pulses presented will suppress flowing fluid provided it has a long- $T_2$  and is within the off-resonance tolerance of the pulses. This is shown by the lack of blood signal in Figs. 11 and 12.

The single- and dual-band suppression pulses are not robust to variations in  $B_1$ . We investigated using adiabatic or composite pulses. An adiabatic half-passage can be used for saturation, but has very poor off-resonance characteristics. Using a BIR-4 pulse solves the off-resonance

problem (29), but destroys all short- $T_2$  magnetization. Composite pulses require multiple excitations that also destroy most of the short- $T_2$  signal (30).

There are alternatives to using a dual-band suppression pulse for fat suppression. One example would be using frequency-selective IR to null fat in conjunction with a single-band suppression pulse. This might improve short- $T_2$  signal slightly, but the imaging sequence must include the inversion time. Image subtraction could also be used to suppress fat, but the SNR would be degraded by a factor of  $1/\sqrt{2}$  because the second echo time image only adds noise to the short- $T_2$  components.

Long- $T_2$  suppression pulses offer significant contrast improvements in 3D UTE imaging, where signal from the whole volume in the center of  $k$ -space can inhibit the dynamic range. This makes it difficult to get contrast from short- $T_2$  species because the long- $T_2$  species dominate most of the dynamic range. The suppression also sparsifies the signal, which allows for higher undersampling ratios because there will be fewer tissues with signal to cause artifacts. This allows for scan time reductions, which are especially beneficial in 3D radial imaging.

In some applications, long- $T_2$  suppression may not be required but short- $T_2$  contrast enhancement would be beneficial. To achieve this, a suppression pulse could be applied, but with a less than  $\pi/2$  flip angle, creating a contrast preparation pulse. The long- $T_2$  species would be partially suppressed, improving the short- $T_2$  contrast. Less short- $T_2$  signal would be lost with a contrast pulse compared to a suppression pulse.

## CONCLUSION

We have introduced a set of new single-band long- $T_2$  suppression pulses designed using the SLR pulse design algorithm. We have derived an inherent trade-off between short- $T_2$  signal and bandwidth, meaning that long- $T_2$  suppression pulses should be narrow bandwidth and will be susceptible to off-resonance artifacts. Our single-band pulses are more robust to off-resonance than rectangular pulses while maintaining the same  $T_2$  contrast. They do not introduce any significant  $T_1$  selectivity. We have also introduced dual-band long- $T_2$  suppression pulses that additionally suppress fat with minimal damage to short- $T_2$  species. The suppression pulse simulation results were confirmed by  $T_2$  phantom experiments. Single-band pulses used in brain UTE imaging showed improvement over rectangular pulses and subtraction. Dual-band pulses were applied in ankle and knee UTE imaging, creating excellent contrast for tendons, menisci, and other short- $T_2$  tissues. These are just a few of the potential applications for these suppression pulses in short- $T_2$  imaging.

## Acknowledgments

We thank Brian Hargreaves for his MATLAB software and Chuck Cunningham for assistance with the  $\text{MnCl}_2$  phantoms.

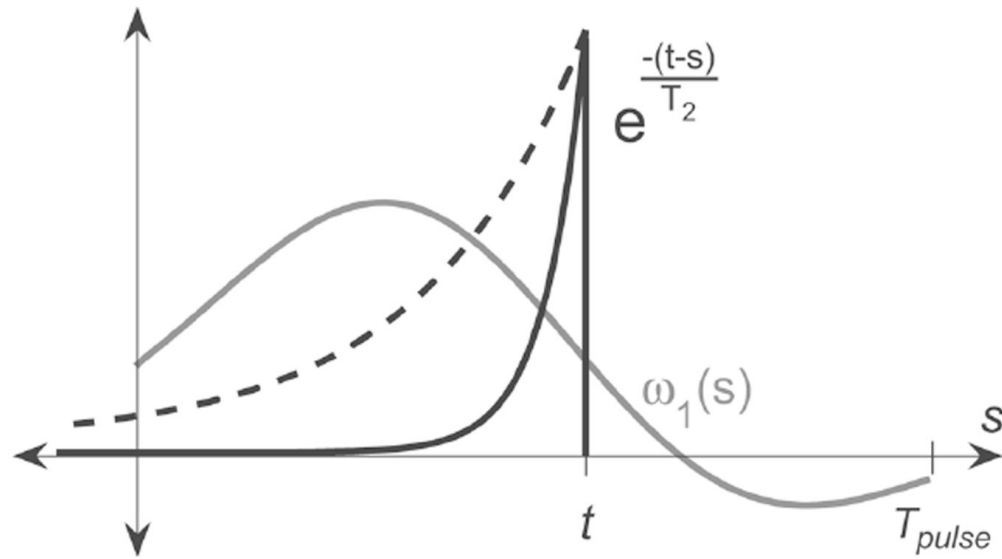
Grant sponsor: GE Medical Systems; Grant sponsor: NIH; Grant number: 1R01-EB002524.

## References

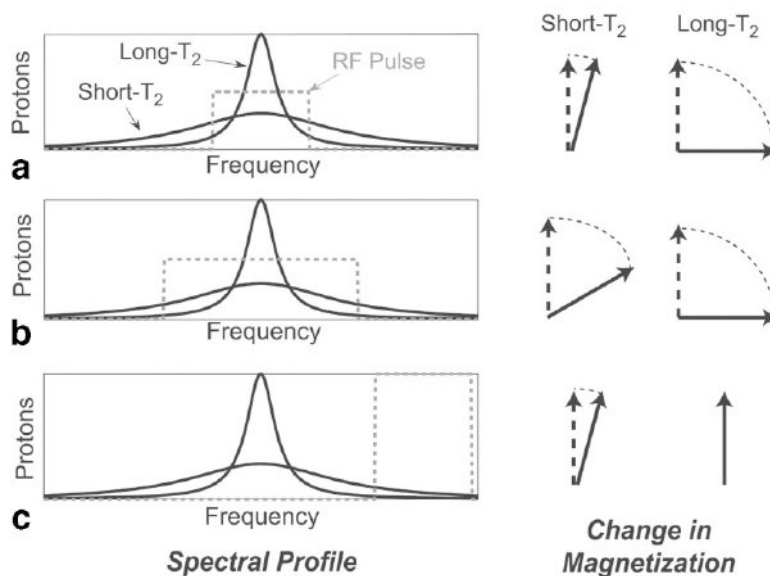
1. Gatehouse P, Bydder G. Magnetic resonance imaging of short  $T_2$  components in tissue. *Clin Radiol* 2003;58:1–19. [PubMed: 12565203]
2. Robson MD, Gatehouse PD, Bydder M, Bydder GM. Magnetic resonance: an introduction to ultrashort TE (UTE) imaging. *J Comput Assist Tomogr* 2003;27:825–846. [PubMed: 14600447]
3. Balcom BJ, MacGregor RP, Beyea SD, Green DP, Armstrong RL, Bremner TW. Single-point ramped imaging with  $T_1$  enhancement (SPRITE). *J Magn Reson A* 1996;123:131. [PubMed: 8980075]

4. Fernandez-Seara MA, Wehrli SL, Wehrli FW. Multipoint mapping for imaging of semi-solid materials. *J Magn Reson* 2003;160:144–150. [PubMed: 12615156]
5. Brittain, JH.; Shankaranarayanan, A.; Ramanan, V.; Shimakawa, A.; Cunningham, CH.; Hinks, S.; Francis, R.; Turner, R.; Johnson, JW.; Nayak, KS.; Tan, S.; Pauly, JM.; Bydder, GM. Ultra-short TE imaging with single-digit (8 $\mu$ s) TE. Proceedings of the 12th Annual Meeting of ISMRM; Kyoto, Japan. 2004. p. 629
6. Nayak, KS.; Pauly, JM.; Gold, GE.; Nishimura, DG. Imaging ultra-short T2 species in the brain. Proceedings of the 8th Annual Meeting of ISMRM; Denver, CO, USA. 2000. p. 509
7. Waldman A, Rees JH, Brock CS, Robson MD, Gatehouse PD, Bydder GM. MRI of the brain with ultra-short echo-time pulse sequences. *Neuroradiology* 2003;45:887–892. [PubMed: 14508620]
8. Chappell KE, Patel N, Gatehouse PD, Main J, Puri BK, TaylorRobinson SD, Bydder GM. Magnetic resonance imaging of the liver with ultrashort TE (UTE) pulse sequences. *J Magn Reson Imaging* 2003;18:709–713. [PubMed: 14635156]
9. Reichert IL, Benjamin M, Gatehouse PD, Chappell KE, Holmes J, He T, Bydder GM. Magnetic resonance imaging of periosteum with ultrashort TE pulse sequences. *J Magn Reson Imaging* 2004;19:99–107. [PubMed: 14696226]
10. Bergin CJ, Pauly JM, Macovski A. Lung parenchyma: projection reconstruction MR imaging. *Radiology* 1991;179:777–781. [PubMed: 2027991]
11. Bergin CJ, Noll DC, Pauly JM, Glover GH, Macovski A. MR imaging of lung parenchyma: a solution to susceptibility. *Radiology* 1992;183:673–676. [PubMed: 1584917]
12. Gold GE, Pauly JM, Macovski A, Herfkens RJ. MR spectroscopic imaging of collagen: tendons and knee menisci. *Magn Reson Med* 1995;34:647–654. [PubMed: 8544684]
13. Robson MD, Benjamin M, Gishen P, Bydder GM. Magnetic resonance imaging of the Achilles tendon using ultrashort TE (UTE) pulse sequences. *Clin Radiol* 2004;59:727–735. [PubMed: 15262548]
14. Gold GE, Thedens DR, Pauly JM, Fechner KP, Bergman G, Beaulieu CF, Macovski A. MR imaging of articular cartilage of the knee: new methods using ultrashort TEs. *AJR Am J Roentgenol* 1998;170:1223–1226. [PubMed: 9574589]
15. Robson MD, Gatehouse PD, So PW, Bell JD, Bydder GM. Contrast enhancement of short T2 tissues using ultrashort TE (UTE) pulse sequences. *Clin Radiol* 2004;59:720–726. [PubMed: 15262547]
16. Robson MD, Gatehouse PD, Bydder GM, Neubauer S. Human imaging of phosphorus in cortical and trabecular bone in vivo. *Magn Reson Med* 2004;51:888–892. [PubMed: 15122669]
17. Robson MD, Tyler DJ, Neubauer S. Ultrashort TE chemical shift imaging (UTE-CSI). *Magn Reson Med* 2005;53:267–274. [PubMed: 15678544]
18. Nielsen HTC, Gold GE, Olcott EW, Pauly JM, Nishimura DG. Ultra-short echo-time 2D time-of-flight MR angiography using a half-pulse excitation. *Magn Reson Med* 1999;41:591–599. [PubMed: 10204884]
19. Wansapura JP, Daniel BL, Pauly JM, Butts K. Temperature mapping of frozen tissue using eddy current compensated half excitation RF pulses. *Magn Reson Med* 2001;46:985–992. [PubMed: 11675651]
20. Vidarsson L, Conolly SM, Lim KO, Gold GE, Pauly JM. Echo time optimization for linear combination myelin imaging. *Magn Reson Med* 2005;53:398–407. [PubMed: 15678534]
21. Pauly, JM.; Conolly, SM.; Macovski, A. Suppression of long-T<sub>2</sub> components for short-T<sub>2</sub> imaging. Proceedings of the 10th Annual Meeting of SMRI, New York; New York, USA. April, 1992; p. 330
22. Sussman MS, Pauly JM, Wright GA. Design of practical T2-selective RF excitation (TELEX) pulses. *Magn Reson Med* 1998;40:890–899. [PubMed: 9840834]
23. Pauly J, Le Roux P, Nishimura D, Macovski A. Parameter relations for the Shinnar–Le Roux selective excitation pulse design algorithm. *IEEE Trans Med Imaging* 1991;10:53–65. [PubMed: 18222800]
24. Hinshaw WS, Lent AH. An introduction to NMR imaging: From the Bloch equation to the imaging equation. *Proc IEEE* 1983;71:338–350.
25. Rabiner, LR.; Gold, B. Theory and application of digital signal processing. Englewood Cliffs, NJ: Prentice-Hall; 1975.
26. Karam LJ, McClellan JH. Complex Chebyshev approximation for FIR filter design. *IEEE Trans Circuits Syst II Analog Digital Signal Process* 1995;42:207–216.

27. Boada FE, Gillen JS, Shen GX, Chang SY, Thulborn KR. Fast three dimensional sodium imaging. *Magn Reson Med* 1997;37:706–715. [PubMed: 9126944]
28. Xia Y, Moody JB, Alhadlaq H. Orientational dependence of T2 relaxation in articular cartilage: a microscopic MRI (microMRI) study. *Magn Reson Med* 2002;48:460–469. [PubMed: 12210910]
29. Garwood M, Ke Y. Symmetric pulses to induce arbitrary flip angles with compensation for RF inhomogeneity and resonance offsets. *J Magn Reson* 1991;94:511–525.
30. Larson, PEZ.; Nishimura, DG. Robust long-T2 suppression pulses. Proceedings of the 12th Annual Meeting of ISMRM; Kyoto, Japan. 2004. p. 2653

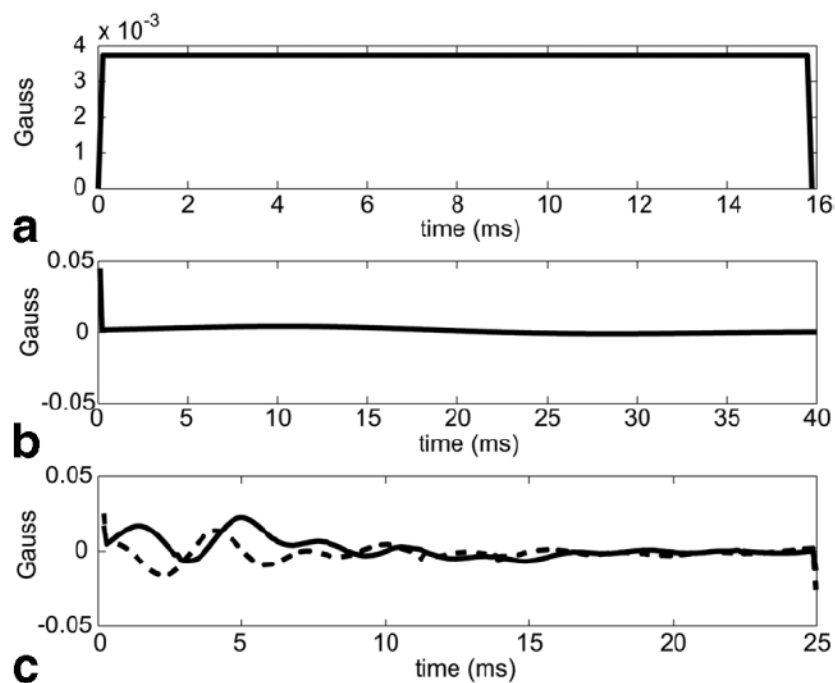
**FIG. 1.**

Graphical illustration of the convolution integral in Eq. [3]. When the RF pulse variations are slower than the  $T_2$  exponential decay,  $\omega_1(s)$  is approximately constant and can be removed from the integral, as is done to derive Eq. [6]. This approximation is valid for shorter  $T_2$  values (solid line), but will not hold for longer  $T_2$  values (dashed line).

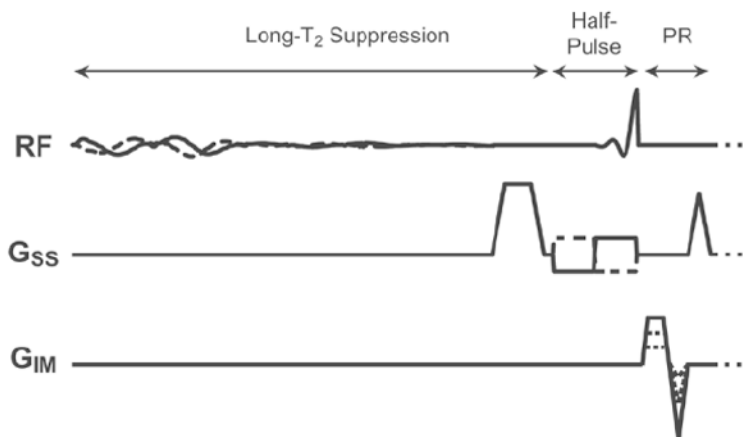


**FIG. 2.** Spectral linewidth (proportional to  $T_2$ ) and RF pulse bandwidth determine excitation (Eq. [8]). (a) Narrow bandwidth (dashed line) RF pulse that overlaps with the majority of the long- $T_2$  spectrum but only a small fraction of the short- $T_2$  spectrum. The long- $T_2$  species is excited more by the pulse than the short- $T_2$  species. (b) Wide bandwidth (dashed line) RF pulse that overlaps with both long- and short- $T_2$  spectra, thus exciting both. (c) Magnetization transfer (MT) pulses applied off-resonance primarily excite short- $T_2$  species.





**FIG. 3.** Long- $T_2$  suppression pulses. (a) 16-ms rectangular suppression pulse. (b) 40-ms TBW = 2.4 single-band suppression pulse. (c) 25-ms dual-band suppression pulse with 80-Hz water suppression bandwidth and 140-Hz suppression centered at -255 Hz for fat suppression—both real (solid line) and imaginary (dashed line) components are shown.

**FIG. 4.**

2D UTE imaging sequence. The long- $T_2$  suppression pulse along with a dephasing gradient is played out before the half-pulse excitation. The slice-select gradient is inverted (dashed-line) between acquisitions to turn the half-pulse into a full pulse. A slice prephasing gradient is also included to allow for acquisition of off-isocenter slices. A projection reconstruction (PR) readout is used, and the above sequence is repeated every TR. In a 3D acquisition, the half-pulse and slice-select gradient are replaced by a hard pulse, and a twisted PR trajectory (27) is used.

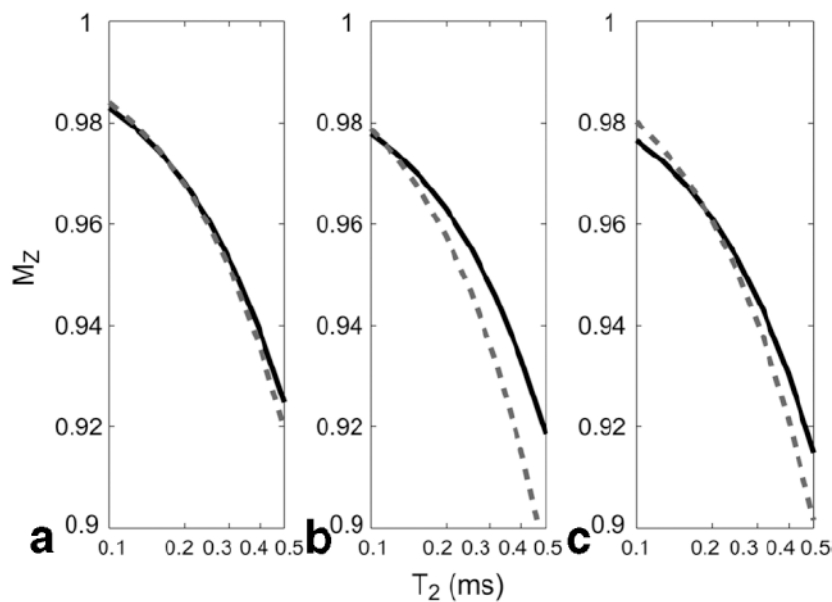


**FIG. 5.**  $T_2$  profile from Bloch equation simulations (solid lines) and the approximation derived in Eq. [7] (dashed lines). (a) 16-ms rectangular pulse. (b) 32-ms TBW = 2 pulse. (c) 64-ms TBW = 4 pulse. The approximation and simulation agree reasonably well for each of the three pulse shapes over the  $T_2$  ranges shown, but the approximation degrades as  $T_2$  increases.

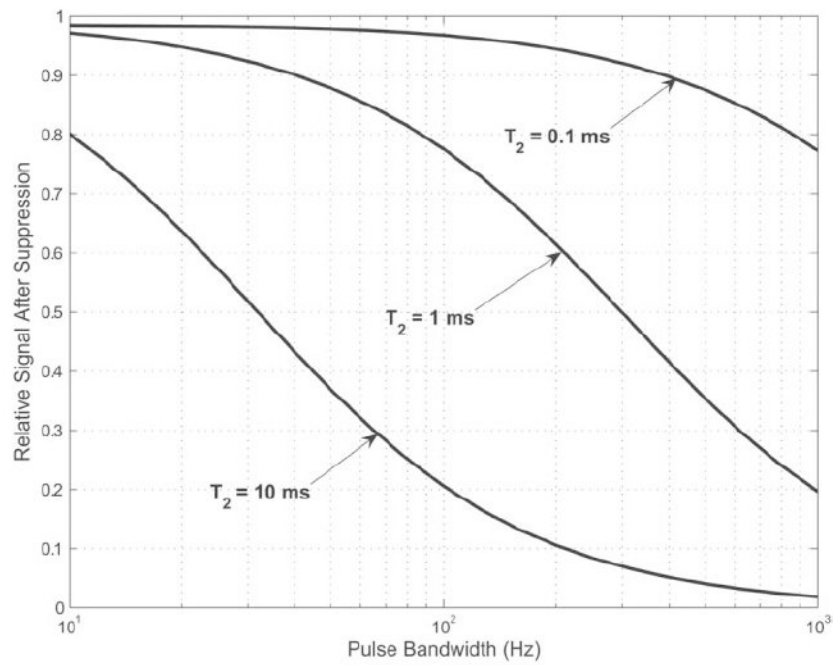


**FIG. 6.** Simulation results for the longitudinal magnetization remaining after single-band suppression pulses of different bandwidths for various  $T_2$  values. As the pulse bandwidth increases, the signal remaining after suppression decreases, as predicted by Eq. [8]. As  $T_2$  increases, the signal also decreases.

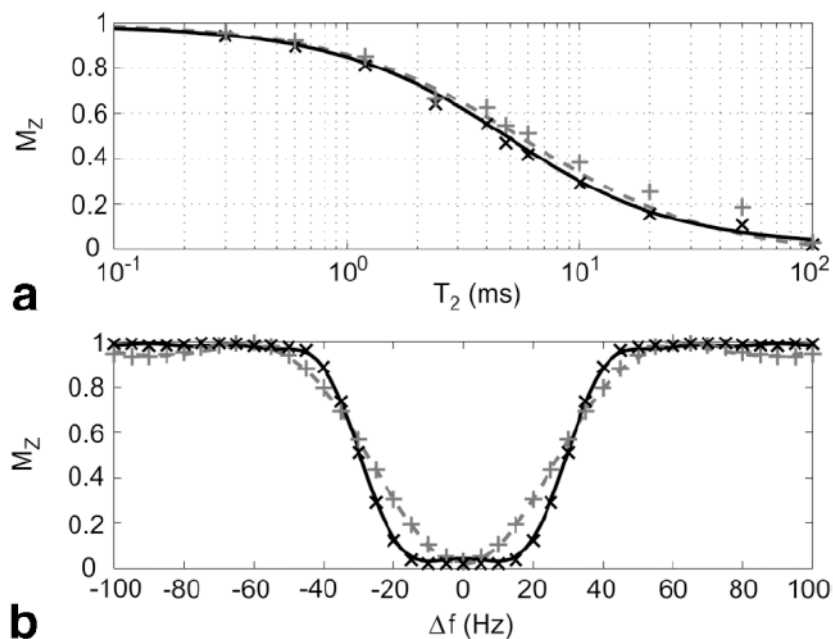


**FIG. 7.** Simulation and phantom experiment results comparing the 16-ms rectangular (dashed line, +) and 40-ms TBW = 2.4 single-band (solid line, ×) suppression pulses shown in Figs. 3a and b. **(a)** On-resonance  $T_2$  profiles. **(b)** Off-resonance profiles for  $T_2 = 100$  ms. The data show that the pulses have nearly identical  $T_2$  profiles, but the single-band pulse off-resonance performance is superior. The phantom data agrees well with the simulations, with the exception of less than expected suppression for  $T_2 > 10$  ms phantoms with the rectangular pulse.

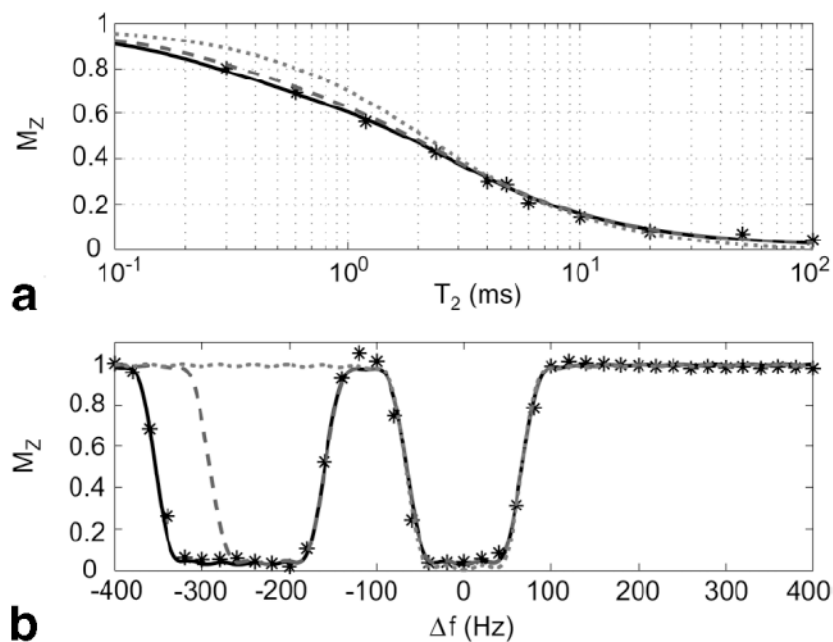


**FIG. 8.** Effect of adding a fat suppression bands. **(a)** On-resonance  $T_2$  profile. **(b)** Off-resonance profile for  $T_2 = 100$  ms. The dual-band pulse used in vivo, shown in Fig. 3c, is represented by the solid line (simulations) and \* (experiments). Using a pulse with a narrower fat suppression band (dashed line, simulated data) has only a small effect on the short- $T_2$  signal. When compared to a 25-ms TBW = 3.4 single-band pulse (dotted line, simulated data), which has the same water suppression bandwidth, the dual-band pulses have approximately 10% additional signal loss for  $T_2 < 1$  ms.



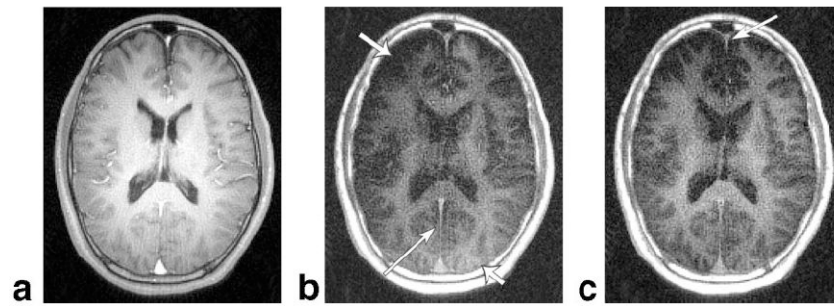


**FIG. 9.** UTE Brain images with and without long- $T_2$  suppression. (a) Unsuppressed image. (b) 16-ms rectangular suppression pulse. (c) 40-ms TBW = 2.4 single-band suppression pulse. With the suppression pulses, short- $T_2$  components in the white matter, likely from myelin, are visible, as is the falx cerebri (long, thin arrows). The rectangular pulse suppression in (b) is variable across the slice (short, fat arrows), while the single-band pulse produces consistent suppression in (c).

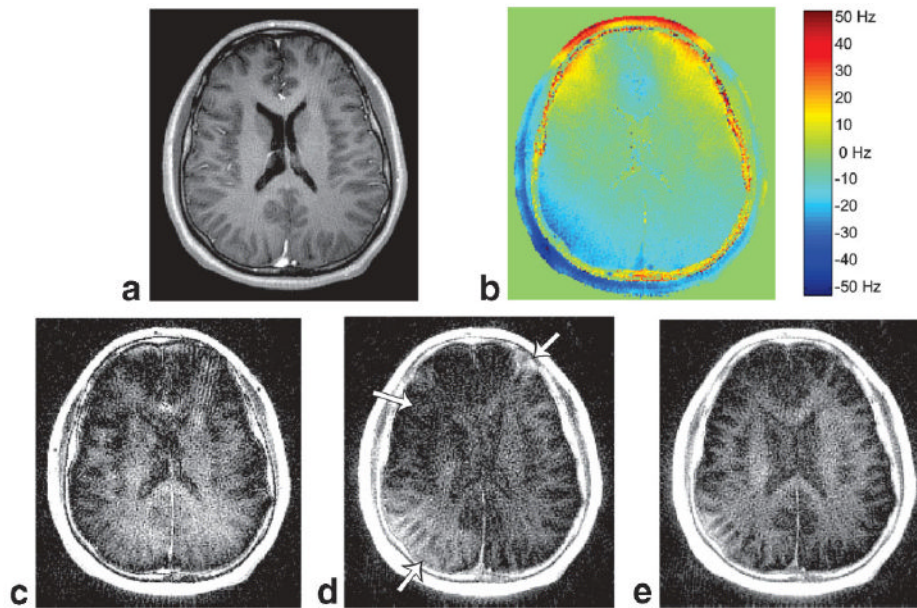


**FIG. 10.** Brain images with various long- $T_2$  suppression techniques. (a) Unsuppressed image. (b)  $B_0$  field map. (c) Subtraction suppression using a TE = 9.7 ms image. (d) 16-ms rectangular suppression pulse. (e) 40-ms TBW = 2.4 single-band suppression pulse. The failure with the rectangular suppression pulse (arrows in (d)) roughly corresponds to off-resonance frequency, shown in (b), especially as this approaches  $\pm 20$  Hz. The subtraction image (c) is also inconsistent, while the single-band suppression pulse (e) produces the most consistent suppression.

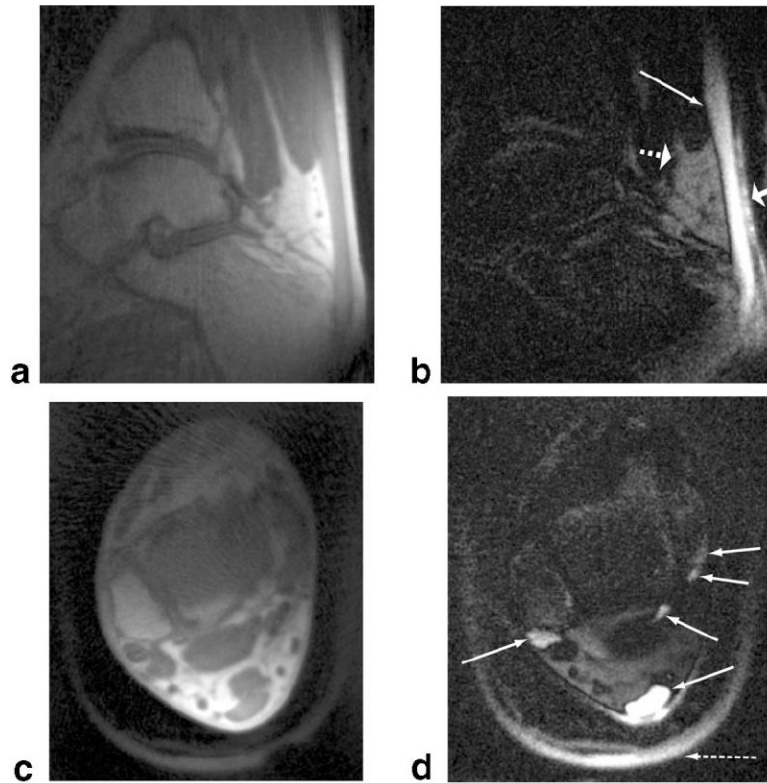


**FIG. 11.** 3D UTE ankle images. Sagittal slice (a) without suppression and (b) with a dual-band long- $T_2$  suppression pulse. Axial slice (c) without suppression and (d) with suppression. The suppression significantly improves the contrast of the tendons, such as the Achilles' tendon in (b) and (d), and the peroneal, flexor hallucis longus, flexor digitorum longus, and tibialis posterior tendons in (d) (long, thin arrows). The plastic boot holding the ankle can also be seen (long, dashed arrow in (d)). Unsuppressed signal in the fat pad anterior to the Achilles' tendon (short, dashed arrow in (b)) may be due to short- $T_2$  components in the fat or suppression failure. Posterior to the Achilles' tendon there is also either failed suppression and/or signal from collagen in the skin (short, solid arrow in (b)).

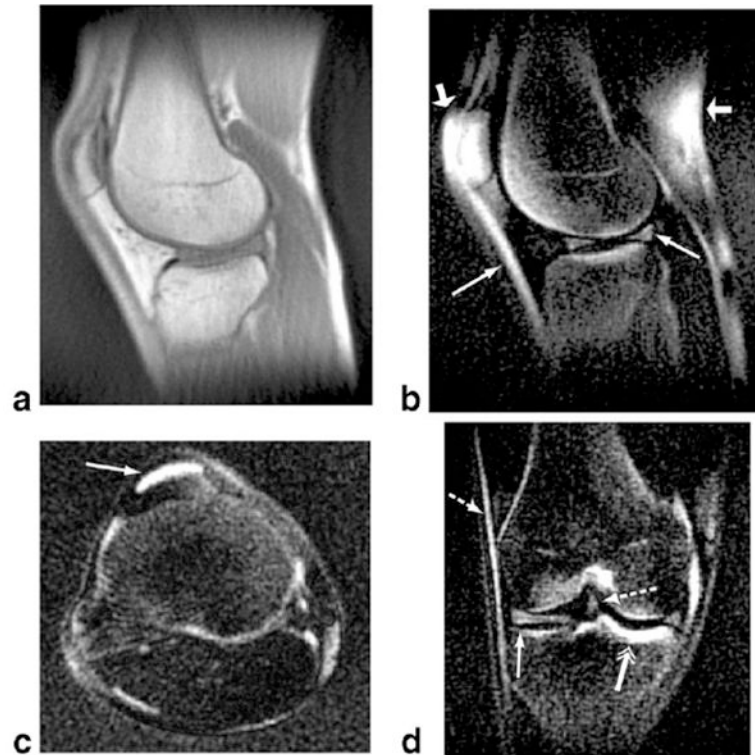


**FIG. 12.** 3D UTE knee images. Sagittal slice (a) without suppression and (b) a dual-band long- $T_2$  suppression pulse. (c) Axial and (d) coronal slices with suppression. The suppression enhances the contrast of the short- $T_2$  structures. The menisci and patellar tendon are particularly visible in (b), (c), and (d) (long, thin arrows). (d) also shows the iliotibial band and the anterior cruciate ligament (dashed arrows), as well as thickened tibial cortex in the weight-bearing region of the knee (double arrow). There is some fat suppression failure around the patella (short, fat arrows in (b)).